Science Bulletin 64 (2019) 669–678

Contents lists available at ScienceDirect

Science Bulletin

journal homepage: www.elsevier.com/locate/scib

Science Bulletin
www.scibull.com

Article

Promoting ring-opening efficiency for suppressing toxic intermediates during photocatalytic toluene degradation via surface oxygen vacancies

Xing'an Dong [a,b], Wen Cui [a], Hong Wang [a,b], Jieyuan Li [c], Yanjuan Sun [a], Haiqiang Wang [d], Yuxin Zhang [e], Hongwei Huang [f], Fan Dong [a,b,*]

[a] Engineering Research Center for Waste Oil Recovery Technology and Equipment of Ministry of Education, Chongqing Key Laboratory of Catalysis and New Environmental Materials, College of Environment and Resources, Chongqing Technology and Business University, Chongqing 400067, China
[b] Research Center for Environmental Science & Technology, Institute of Fundamental and Frontier Sciences, University of Electronic Science and Technology of China, Chengdu 611731, China
[c] College of Architecture and Environment, Sichuan University, Chengdu 610065, China
[d] Department of Environmental Engineering, Zhejiang University, Hangzhou 310027, China
[e] State Key Laboratory of Mechanical Transmissions, College of Materials Science and Engineering, Chongqing University, Chongqing 400044, China
[f] National Laboratory of Mineral Materials, School of Materials Science and Technology, China University of Geosciences, Beijing 100083, China

ARTICLE INFO

Article history:
Received 10 February 2019
Received in revised form 1 April 2019
Accepted 3 April 2019
Available online 12 April 2019

Keywords:
Photocatalysis
Oxygen vacancies
Toluene
Rate-determining step
In situ DRIFTS

ABSTRACT

Aromatic ring-opening process is well recognized as the rate-determining step for catalytic toluene degradation. In photocatalytic toluene degradation, the toxic intermediates with harmful effects may be generated. To clarify the precise reaction mechanism and control the toxic intermediates generation, a closely combined *in situ* DRIFTS and DFT calculation is utilized to address these important issues. We construct the BiOCl with oxygen vacancies (OVs) and reveal the structure of OVs. The defect level caused by oxygen vacancies could promote the light adsorption and charge separation, which further boosts the activation of ring-opening species and enhances the generation process of free radicals. The reaction energy barriers of four possible ring-opening processes on defective BiOCl (OVBOC) are all declined in comparison with perfect BiOCl (BOC). The existence of oxygen vacancies could smooth the rate-determining step so the ring-opening efficiency of photocatalytic toluene degradation is highly increased. Most importantly, the methyl species would be further oxidized and tend to open the benzene-ring at benzoic acid on BOC while the ring would be broken at the benzyl alcohol on OVBOC. These results indicate that the toluene degradation pathway is shortened via the surface OVs, which enables the production of radicals with high oxidation capability for the accelerated chain scission of the ring-opening intermediates. Finally, the efficiency of the key ring-opening process could be enormously improved and toxic intermediates are effectively restrained. The present work could provide new insights into the design of high-performance photocatalysts for efficient and safe degradation of VOCs in air.

1. Introduction

Volatile organic compounds (VOCs), as a kind of toxic substance in air, could pose serious damage to human health [1,2]. As one of typical VOCs, toluene is utilized as an organic solvent in adhesives and paints in the past few years and is likely to be emitted from building material to indoor environment. The VOCs emission has significantly affected the living environment (like sick house syndrome) and the atmospheric environment (like photochemical smog) [3]. To ease the environmental problems caused by VOCs, adsorbed filters with activated carbon, zeolites or diatomaceous earth are extensively used in the market for removing VOCs. The catalytic combustion technology has all been applied in degradation of VOCs at relatively high temperature [4,5]. Nevertheless, to achieve the better air cleaning effectiveness at mild conditions, semiconductor photocatalysts operated at room temperature can be applied to completely mineralized VOCs into CO_2 and H_2O via a radicals-mediated oxidation reaction [6–9].

Many reports have been published on the photocatalytic degradation of VOCs, however, most of them focus solely on the photocatalytic removal performance of the target pollutants. The selectivity of photocatalytic conversion of VOCs to harmless final product along with control of the toxic intermediates during the reaction process has been largely ignored. The issue is the key to application and should be worth receiving high attention [10–14]. Some progresses have revealed that the reaction intermediates, such as aromatic oxides, epoxides, peroxides, and polyhy-

* Corresponding author.
E-mail address: dfctbu@126.com (F. Dong).

https://doi.org/10.1016/j.scib.2019.04.020

droxylated compounds have high toxicity [15]. Furthermore, toxic intermediates produced through the ring-opening process should be also concerned along with the intermediates products containing an aromatic ring. For instance, muconaldehyde, an α,β-unsaturated diene dialdehyde, resulting from ring opening, is proposed as a hematotoxic intermediate during aromatic ring-opening process [16–18]. Hence, elevating ring-opening efficiency and accelerating the chain scission from ring-opening intermediates would be effective strategies for the inhibition of toxic intermediates during the degradation process.

The surface oxygen vacancies (OVs) can serve as the active sites for activating small molecules on the photocatalyst surface, which are of vital importance to enhance the performance in wastewater remediation, artificial synthesis, water oxidation and gaseous pollutants oxidation [19–27]. The OVs possess excess localized electrons and coordinatively unsaturated feature, thus they can provide specific sites to firmly bind with small molecules, then facilitating subsequent molecules activation by localized electrons [28–31]. Abundant active radicals would be generated on the catalyst surface to participate in photocatalytic reactions. The pollutant molecules can also be adsorbed on the defective site and then get activated subsequently via the electrons exchange between the pollutant and the substrate. As a result, the conversion of activated pollutant molecules can be accelerated thermodynamically via the light induced radical oxidation [32–34].

To realize the goal of elevating ring-opening efficiency and accelerating the chain scission of ring-opening intermediates simultaneously, the OVs have been constructed on the surface of BiOCl (OVBOC) to strengthen the adsorption and activation of O_2, H_2O and toluene molecules. The activation of O_2 and H_2O on catalyst surface enables the formation of more reactive radicals with higher oxidizing capability [35]. For the toluene ring-opening process, the methyl is oxidized through the pathway of toluene → benzyl alcohol → benzaldehyde → benzoic acid before opening the aromatic ring [18]. Furthermore, the reaction energy barriers of the ring-opening processes on OVBOC are declined. The OVs reduce the reaction activation energy of the rate-determining step so that the ring-opening efficiency of photocatalytic toluene degradation can be well boosted. Most importantly, it is verified by the *in situ* DRIFS spectra that the methyl species would be further oxidized and tend to open the benzene ring at benzoic acid on BOC while at benzyl alcohol on OVBOC. The production of more CO_2 product on OVBOC indicates that the ring-opening efficiency is higher than that on BOC. Own to the more efficient production of radicals, the ring-opening intermediates, such as unsaturated long chain enol, can be broken into final product CO_2 where the process is associated with little toxic products accumulation. Our work could provide a new strategy to achieve enhanced photocatalytic ring-opening efficiency and toxic intermediates control for safe air purification.

2. Experimental

2.1. Materials and catalyst synthesis

2.1.1. Synthesis of BiOCl with OVs (OVBOC)

All chemicals we used in this work were analytical grade without any further treatment. We synthesized OVs-containing BiOCl with (0 0 1) facet exposures by using the solvothermal-induced hot ethylene glycol reduction. In a typical procedure, 2 mmol Bi $(NO_3)_3{\cdot}5H_2O$ and stoichiometric amounts of KCl were added into 60 mL ethylene glycol solution. The mixture was stirred for 0.5 h at room temperature, and then poured into a 100 mL Teflon-lined stainless autoclave. Subsequently, the autoclave was heated at 160 °C for 12 h, and then cooled down to room temperature. The resulting precipitates were collected and washed with deionized water and then ethanol and dried at 60 °C in vacuum.

2.1.2. Synthesis of OV-free BiOCl microspheres (BOC)

For comparison, the counterpart sample without oxygen vacancies was synthesized [27]. In our experiment, 0.5 g of OVBOC was mixed with H_2O_2 (1 mL, 10%) and dried under 60 °C, subsequently the dried powder was washed with deionized water and ethanol and dried at 60 °C in vacuum and then repeated the above H_2O_2 treating process for one time. After that, heating the H_2O_2 treated BiOCl at 300 °C in the O_2 atmosphere for 4 h to re-oxidize the surface.

2.2. Characterization

The crystal phases of the samples were analyzed by X-ray diffraction (XRD) with Cu Kα radiation (model D/max RA, Rigaku Co., Japan). X-ray photoelectron spectroscopy (XPS) with Al Kα X-rays (Thermo ESCALAB 250, USA) was used to investigate the surface properties. The morphology and structure of the samples were examined by scanning electron microscopy (SEM, model JSM-6490, JEOL, Japan) and transmission electron microscopy (TEM, JEM-2010, Japan). The UV-vis diffuse-reflectance spectrometry (UV-vis DRS) spectra were obtained for the dry-pressed disk samples using a scanning UV-vis spectrophotometer (UV2550, Shimadzu, Japan) equipped with an integrating sphere assembly, using 100% $BaSO_4$ as the reflectance sample. Photoluminescence (PL) studies (F-7000, HITACHI, Japan) were conducted to investigate the optical properties of the samples. Steady and time-resolved fluorescence emission spectra were recorded at room temperature with a fluorescence spectrophotometer (Edinburgh Instruments, FLSP-920, UK). Electron spin resonance (ESR) of radicals spin-trapped by 5,5-dimethyl-1-pyrroline N-oxide (DMPO) were recorded on a JES FA200 spectrometer. Samples for ESR measurement were prepared by mixing the samples in a 40 mmol/L DMPO solution tank (aqueous dispersion for DMPO-$^{\bullet}OH$ and methanol dispersion for DMPO-$^{\bullet}O^{2-}$) and irradiated with UV light. Electron paramagnetic resonance (EPR) measurements were carried out on a Bruker ESP 500 spectrometer (Germany).

2.3. Evaluation of UV-light photocatalytic activity

The photocatalytic efficiency was investigated towards the toluene purification at 1 L/min in a house-customized continuous flow reaction system (Scheme S1 online). The rectangular reactor was made of polymeric glass and covered by quartz class. The as-prepared sample (0.4 g) was dispersed on four glass sheets for photocatalytic testing. A 300 W UV lamp (λ = 365 nm) was vertically placed above the reactor. After the adsorption-desorption equilibrium was achieved, the lamp was turned on. The toluene gas was obtained from a compressed gas cylinder at the concentration of 500 ppm (in N_2) with the flow rate of 100 mL/min. The initial concentration of toluene was diluted to 50 ppm by two separated air flows, respectively wet air at 500 mL/min and dry air at 400 mL/min. The toluene concentration was continuously detected by a gas chromatography (GC 7890 Ⅱ, Techcomp Co. Ltd., China). The toluene removal ratio (η) was calculated as

$$\eta(\%) = (1 - A/A_0) \times 100\%, \quad (1)$$

where A and A_0 depict the toluene peak area in the outlet steam and the feeding stream, respectively.

2.4. In situ DRIFTS study on photocatalytic toluene oxidation process

In situ DRIFTS measurements were conducted using the Tensor II FT-IR spectrometer (Bruker) equipped with an *in situ* diffuse

reflectance cell (Harrick) (Scheme S2 online). Photocatalysts were put into the reaction cell. First, the He gas (50 mL/min) was used to remove the residual hydrocarbons, H_2O and CO_2 under 300 °C. The real-time FT-IR spectrum after ventilation was utilized as background. Then, the reaction mixtures (25 mL/min toluene, 25 mL/min O_2) were introduced into the cell. The toluene adsorption on the catalysts was carried out for 20 min. Next, photocatalysts were illuminated by UV light source (MUA-165) for 1 h. The real-time FT-IR spectra were detected every two minutes. Meanwhile the gas fluxes keep the same (25 mL/min toluene, 25 mL/min O_2). Finally, FT-IR spectra were recorded every two minutes with the same gas fluxes after turning off the light. The IR scanning range was 4,000–600 cm^{-1}. The intervals 3,700–2,500 cm^{-1} and 2,200–1,300 cm^{-1} were analyzed to present the photocatalytic oxidation process on the catalysts. The pristine data of DRIFTS was further normalized to investigate the species evolution as time proceeded. For a specific species absorbed on the surface, the data of peak heights in both catalysts were extracted. Between the two data columns, the highest value was set to 1 and the lowest one was set to 0. The rest value was respectively calculated from 0 to 1. The normalized data were then described as a function of the DRIFTS time.

2.5. DFT calculations

Spin-polarized DFT-D2 calculations [36] were conducted using the "Vienna ab initio simulation package" (VASP5.4) [37,38], applying a generalized gradient correlation functional [39]. A plane-wave basis set with cut-off energy 450 eV within the framework of the projector-augmented wave method was employed [40,41]. The Gaussian smearing width was set to 0.2 eV. The Brillouin zone was sampled with a $3 \times 3 \times 1$ Monkhorst Pack grid. All atoms were converged to 0.01 eV/Å. Hybrid functional based on the Heyd-Scuseria-Ernzerhof (HSE06) method were applied to estimate the exact band structures [42,43]. The climbing image nudged elastic band (CI-NEB) method was applied to locate the minimum energy pathway of transition state (TS) from the initial state (IS) to its final state (FS) [44]. The obtained electrons of specific atoms and molecules, Δq, were calculated with the Bader method [45], where positive and negative values correspond to electron depletion and accumulation, respectively.

The adsorption energy (E_{ads}) is defined as

$$E_{ads} = E_{tot} - (E_{cat} + E_{mol}), \quad (2)$$

where E_{tot}, E_{cat} and E_{mol} depict the total energy of the adsorption complex, the catalysis and the isolated molecule, respectively.

3. Results and discussion

3.1. Structural features of catalyst

Both the two BiOCl samples (BOC and OVBOC) have tetragonal structure with a space group of *P4/nmm* and a *D7 4 h* symmetry according to XRD spectra (JCPDS No. 06-0249, Fig. 1a). The low-temperature electron paramagnetic resonance (EPR) spectra are applied to determine the presence of oxygen vacancies. The typical signal at *g*-value around 2.0 is the typical characteristic of OVs [46], which is significant for OVBOC, indicating the high OVs

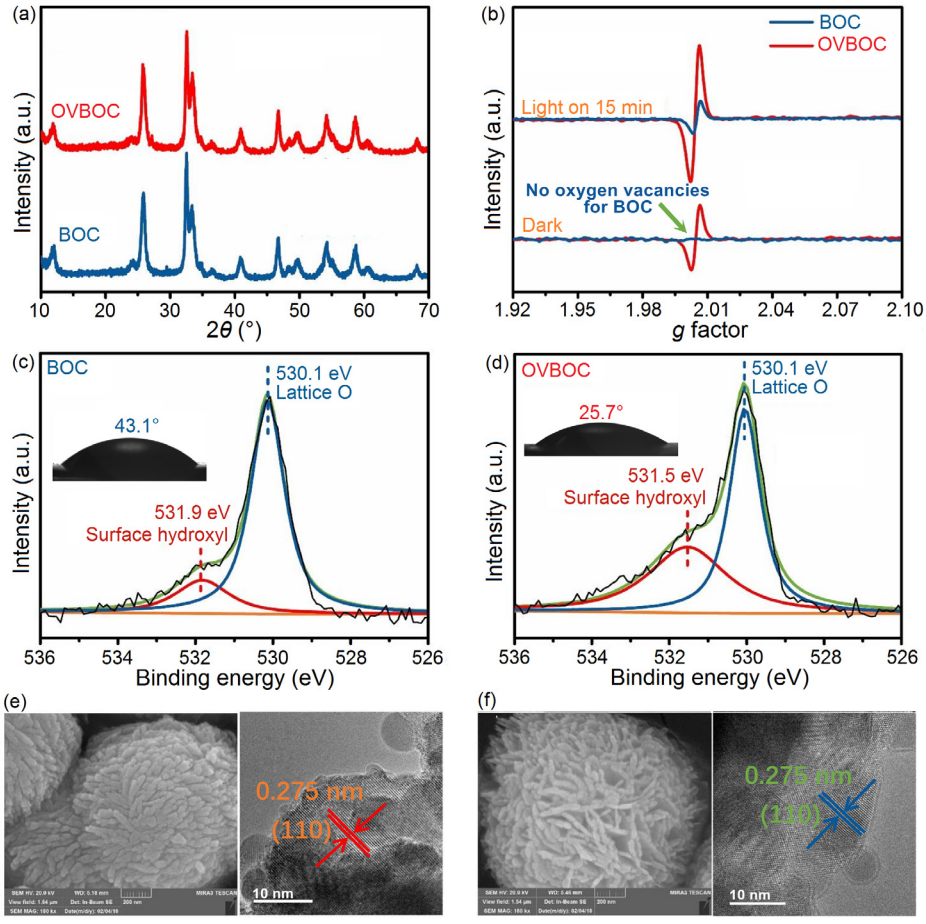

Fig. 1. XRD spectra of BOC and OVBOC (a); EPR spectra of BOC and OVBOC in dark and with UV-light on for 15 mins (b); XPS spectra of O1s of BOC (c) and OVBOC (d), photos of the water droplets on the BOC (c insert) and OVBOC (d insert) surfaces; SEM and TEM images of BOC (e) and OVBOC (f).

concentration in comparison with BOC (Fig. 1b). Under visible light irradiation, the intensified signals can be observed for both BOC and OVBOC, which suggest that the OVs are responsive to visible light, making the light-induced carriers transfer in an extended region.

Because of the water dissociation on the OVs of OVBOC, the increased density of surface hydroxyl groups is detected by XPS. The O 1s spectra of OVBOC show a broader shoulder between 531.0 and 532.0 eV compared with BOC. A shift to lower binding energy of the surface hydroxyl groups in OVBOC can be observed, which is associated with existence of OVs (Fig. 1c and d). The survey scan XPS spectrum is shown in Fig. S1 (online). Enlightened by the above XPS results, we further investigated the different microscopic water-surface interaction modes via macroscopic water adsorption on the catalysts surfaces monitored by *in situ* water contact angle measurements. The BOC is relatively hydrophobic with an initial water contact angle of 43.7°, which is higher than the angle of 25.1° on OVBOC, confirming the strong interaction between water and OVBOC surface. This enhancement indicates the increase of surface hydroxyl groups originating from the H_2O dissociation on OVs of the BiOCl (0 0 1) surface [47–49]. The two BiOCl samples consist of nanoplate microspheres with diameter about 2 μm (Fig. 1e and f, left). Their nanoplates are exposed with {0 0 1} facets according to the analysis of SEM and HRTEM images (Fig. 1e and f, right). Obviously, the H_2O_2 treatment coupled with infrared irradiation method does not affect the phase and morphology of BiOCl.

The theoretical models of perfect and defective crystals of BiOCl are shown in Fig. 2a and b, which are the foundation of further calculations for band structure and electronic structure. As expected, besides exhibiting an absorption tail at around 400 nm for the pristine BOC, the OVBOC shows an additional exponentially decaying absorption tail across the whole UV and visible light region (Fig. 2c). The significantly enhanced light absorption should be ascribed to the formation of oxygen vacancies on the surface of BOC. Subsequently, we employ first-principle DFT to calculate the band structure (density of states; DOS) as shown in Fig. 2d. DFT calculation results reveal that the defect state is formed originating from the 6p orbitals of Bi atoms (Fig. S2 online) and the band gap is also reduced. The contribution of this defect level lowers the photoenergy required for electron transition, benefiting for the electronic excitation, separation, and transformation. So the charge separation efficiency has been improved greatly. This modified band structure directly leads to the highly promoted light adsorption for OVBOC, consistent with their UV–vis DRS spectra (Fig. 2c).

The separation efficiency of photo-generated charges is characterized by photoluminescence spectra (PL) as shown in Fig. 2e. The two samples exhibit a broad emission peak centered at around 380–520 nm, and the PL intensity of OVBOC is much lower than that of BOC. This observation illustrates that the OVs could also increase the separation efficiency of photogenerated charges. The ns-level time-resolved fluorescence spectra are further employed to investigate the charge transfer dynamics over BOC and OVBOC

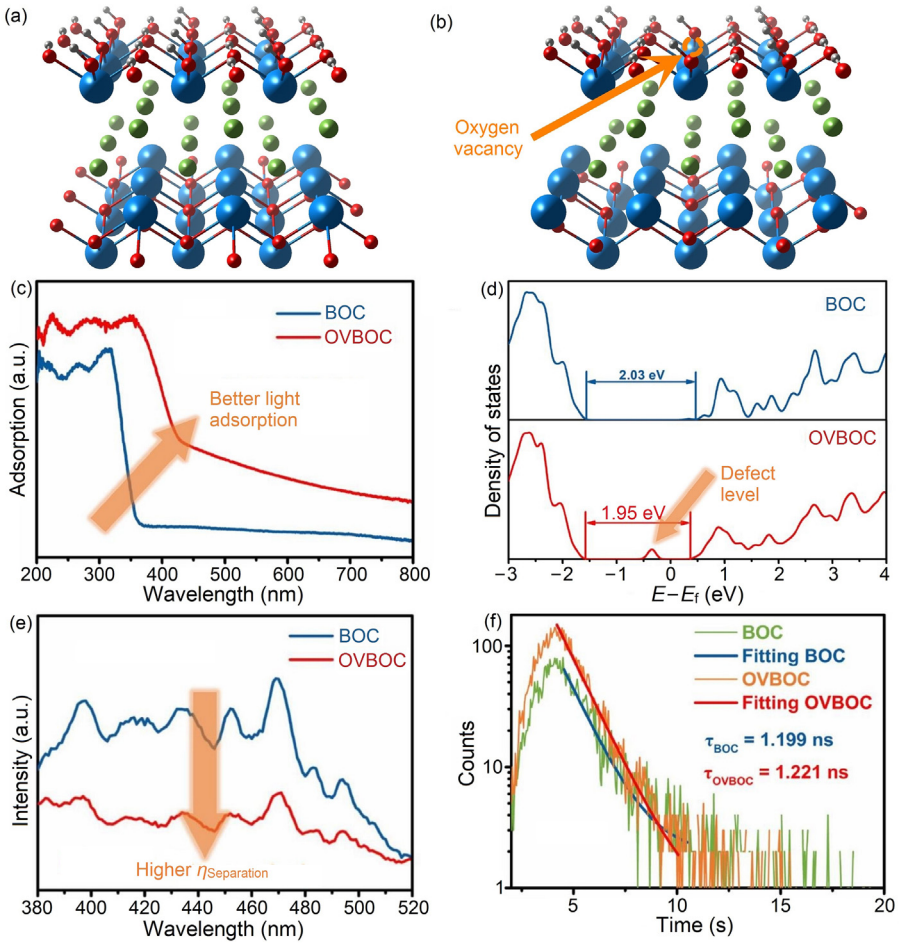

Fig. 2. The optimized crystal structure of BOC (a) and OVBOC (b); UV-vis DRS spectra of BOC and OVBOC (c); the calculated total density of states (TDOS) for pristine surfaces (BOC) and surfaces with oxygen vacancies defects (OVBOC). The Fermi level is set to 0 eV (d); PL spectra of BOC and OVBOC with an excitation wavelength of 360 nm (e); ns-level time-resolved fluorescence spectra surveyed at room temperature of BOC and OVBOC (f).

(Fig. 2f). Interestingly, the lifetime of OVBOC is obviously prolonged in comparison with perfect BOC, which demonstrates that the OVs could effectively store photogenerated electrons and then transfer the electrons to the reactants of O_2 [50,51]. These results imply that the OVs could suppress the electron-hole recombination and guide the charge carriers to the defects sites to enhance the reactant activation.

To clarify reactive oxygen species (ROS) dependent toluene ring-opening oxidation process of BiOCl with OVs under UV light, the ROS ($\cdot O_2^-$, e^- and ·OH) generation and transformation over BOC and OVBOC are investigated. Under 360 nm light illumination, the four strong characteristic peaks (with intensity of 1:1:1:1) for BOC and OVBOC can be observed in Fig. 3a, indicating the mass production of $\cdot O_2^-$ radicals through O_2 reduction by photoexcited electrons. Obviously, the number of $\cdot O_2^-$ radicals produced by OVBOC exceeds those produced by BOC because of the enhanced charge separation and O_2 activation. Meanwhile, as shown in Fig. 3b, more photo electrons scavenger agent can be consumed within 15 min, which is consistent with the trend of $\cdot O_2^-$ production. More importantly, it is found that the potential energy of the valance band (VB) holes is positive enough to directly oxidize H_2O/OH^- into ·OH radicals (Fig. S3 online), which contributes directly to the decomposition of toluene. As the main radical to participate in the toluene ring-opening process, the ·OH radicals are produced by the water oxidation via first proton removal reaction ($H_2O^* + h^+ \rightarrow \cdot OH^* + H^+$) [34]. When UV light is applied to directly excite the BiOCl, strong four-line EPR spectra (with the relative intensities of 1:2:2:1 corresponding to ·OH radicals) can be served over BOC and OVBOC (Fig. 3c). The ·OH signal of OVBOC is much stronger than that of BOC because of the role of the OVs in promoting charge separation and light utilization, H_2O adsorption and dissociation, which in line with the XPS results.

Subsequently, the as-prepared catalysts are applied in oxidation removal of toluene and NO in air under 360 nm UV light irradiation (Fig. 3d). The removal ratios of toluene (64.0%) and NO (43.5%) on OVBOC are both boosted obviously in comparison of the pristine BOC. The highly enhanced photocatalytic activity of OVBOC can be ascribed to the oxygen vacancies that could mediate the formation of the middle gap level, promote the charge separation, and enhance the O_2 and H_2O activation.

In order to better understand relationship between the H_2O dissociation and ·OH production, molecular water adsorption and activation on the BOC and OVBOC (0 0 1) surfaces are simulated (Fig. 4). The H_2O molecules adsorption on the OVs site in the inner layer makes the O atom from H_2O act as a credible hydrogen bond acceptor site for the enhanced outer-layer water adsorption with a moderate hydrogen bond. Therefore, both the higher binding energy for water adsorption in the inner layer and the stronger water hydrogen bond formed in the outer layer could determine the hydrophilicity character on OVBOC. The H—O bonds length of H_2O molecules is enlarged on defective surface no matter how many H_2O molecules are adsorbed on OVBOC. This result implies that the H_2O molecules tend to adsorb on the defective site and get activated to enhance the production of ·OH radicals. The theoretical results are fully consistent with the water contact angle, XPS and ESR results. Correspondingly, one to four O_2 molecules adsorption calculations on the BOC and OVBOC (0 0 1) surfaces are adopted (Fig. S4 online). The adsorbed O_2 molecules possess higher adsorption energy, longer O—O bond length and could capture more electrons, demonstrating that the O_2 molecules could also be activated to $\cdot O_2^-$ on the defective surface.

The electron density of OV is mainly localized at the center of OV surrounding Bi atoms (Fig. S5 online). Thus, the theoretical results have been adopted to suggest that the donation of localized electron from OVs to adsorbed H_2O could directly facilitate the H_2O dissociation into ·OH radicals, which are the primary reactive species for oxidation reaction. For photocatalytic toluene degradation, the ring-opening process is the rate-determination step. The pollutant adsorption and activation is the first step before the ring-opening process. Hence, the DFT is employed to investigate the interaction between toluene and BiOCl surface with and without oxygen vacancy. The adsorption energy for toluene on OVBOC

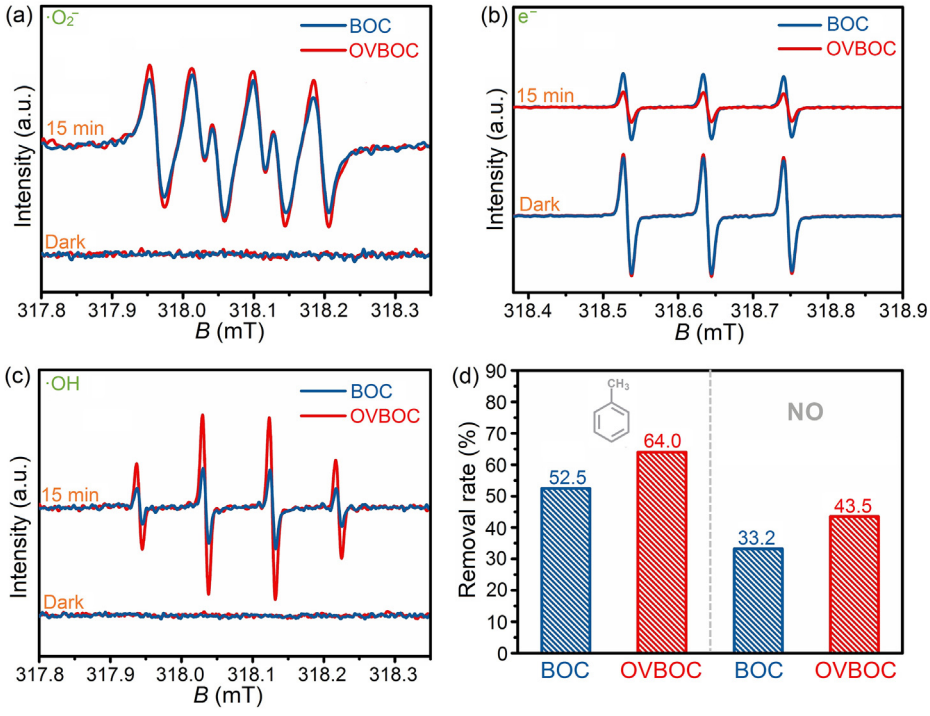

Fig. 3. DMPO ESR spectra in dark and under ultraviolet light (λ = 360 nm) for 15 min, respectively in methanol dispersion for c (a); TEMPO was used as photo electrons scavenger agent (b) and aqueous dispersion for ·OH (c) of BOC and OVBOC; photocatalytic activity comparison of BOC and OVBOC in removal of toluene and NO in air (d).

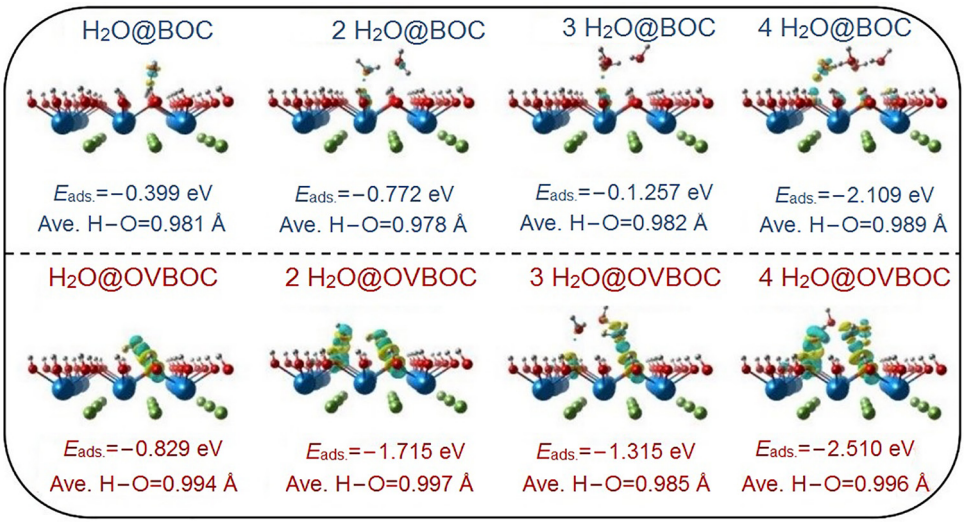

Fig. 4. Calculated adsorption energy and average H—O bond length for one H_2O molecule to four H_2O molecules on BOC (upper row) and OVBOC (under row).

was −0.671 eV, which is much higher than that on BOC (−0.355 eV). This indicates that the oxygen vacancies on the surface are more favorable for the adsorption of toluene molecules.

The oxidation of methyl on toluene follows the route of toluene → benzyl alcohol → benzaldehyde → benzoic acid. This process is calculated on both the perfect and defective surface of BiOCl as shown in Fig. S6 (online) [18]. All the reactions are exothermic processes. This thermodynamic plot could account for the observation that the methyl could be oxidized spontaneously. Obviously, the heat releases of for oxidation reactions (toluene to benzyl alcohol, benzaldehyde to benzoic acid) on the defective surface are higher than that on perfect surface. However, the benzyl alcohol to benzaldehyde process exhibit an opposite trend (−0.532 eV on BOC and −0.119 eV on OVBOC). This result indicates that the toluene tends to transform into benzoic acid on the perfect surface while keeping in benzyl alcohol state on defective surface. In this case, theoretically, the benzene ring-opening process of photocatalytic toluene degradation would be reached at benzoic acid state on BOC and benzyl alcohol state on OVBOC.

In order to get a deeper understanding of the full ring-opening step, the DFT calculations are further carried out on the four feasible reactions oxidized by two ·OH radicals to determine the transition state and the energy barrier (Figs. 5, S7–S9 (online)). Apparently, the thermodynamic energy barriers of four possible ring open steps on OVBOC are much lower than that on BOC. Thus, the ring-opening process on the defective surface is more thermodynamically favorable than that on the perfect surface. This is caused by higher adsorption energies of four benzene compounds (Table 1) that would lead to the higher activation efficiency of the reaction intermediates.

Note that the energy barrier for benzyl alcohol ring-opening on the defective surface is 1.260 eV, which is even lower than the barrier 1.444 eV for the ring-opening for benzoic acid on perfect surface. This could make two oxidation steps with decreased the toxic intermediates accumulation of aromatic oxides and polyhydroxylated compounds and thus open the benzene ring with a lower barrier on defective surface. Above all, the ring-opening efficiency could be enhanced when the ring-opening process is started at benzoic acid state on BOC and benzyl alcohol state on OVBOC.

In order to Figure out the ring-opening step experimentally, the *in situ* DRIFTS, which could dynamically monitor the adsorbed reaction intermediates and products in time sequence, are subsequently carried out to reveal the conversion pathways and reaction mechanism for photocatalytic toluene degradation. As for BOC (Fig. 6a), toluene absorption bands (2,933 cm^{-1}) appear immediately after the toluene molecules contact with BOC at 25 in dark condition [52]. Meanwhile, the chemical adsorbed toluene could be preliminary oxidized into benzyl alcohol (3,459 and 3,568 cm^{-1}) [53], benzaldehyde (1,620 cm^{-1}) [54] and benzoic acid (1,497 cm^{-1}) [55] because of the spontaneous exothermic procedure as theoretically calculated above. Nevertheless, the band of benzene ring at 3,029 cm^{-1} can be observed which reveals that the benzene ring couldn't be opened during the adsorption process [56,57].

On the OVBOC surface (Fig. 6b), toluene (2,883 cm^{-1}), benzyl alcohol (3,468 and 3,576 cm^{-1}), benzaldehyde (1,600 cm^{-1}), benzoic acid (1,498 cm^{-1}) and benzene ring (3,025 cm^{-1}) have been detected during the adsorption process. The increased adsorption band of each peak indicates the gradual accumulation of the species on the surface. Moreover, according to IR spectra in time sequence, the temporal evolution of normalized absorbance for toluene, benzyl alcohol, benzaldehyde and benzoic acid during the adsorption process is illustrated in Fig. 6c. The adsorption quantity of toluene, benzyl alcohol benzaldehyde and benzoic acid on OVBOC are much higher than that on BOC, which can be attributed to the oxygen vacancies as adsorption sites promoting the adsorption of toluene.

After the adsorption equilibrium is achieved, the time-dependent IR spectra on BOC and OVBOC are monitored dynamically under UV light irradiation. As shown in the photocatalytic degradation process on BOC (Fig. 6d), C—H bending vibration in methyl (around 2,950 cm^{-1}) of the toluene, the ν(OH) of benzyl alcohol (about 3,500 cm^{-1}) and ν(C=O) of benzaldehyde (1,650 cm^{-1}) are gradually decreased while ν_{as}(COO) and ν_s(COO) of the benzoic acid (1,377, 1,547 and 1,675 cm^{-1}) are increased. This result implies that the toluene is firstly oxidized to benzoic acid and accumulated on surface under light irradiation. Next, the benzene ring is opened and the unsaturated long chain enol is broken gradually because of the thermodynamic advantage as shown in Fig. S9 (online).

With regard to photocatalytic degradation process on OVBOC (Fig. 6e), the toluene (around 2,950 cm^{-1}) is consumed and benzyl alcohol (3,535 and 3,605 cm^{-1}) is accumulated apparently. Besides,

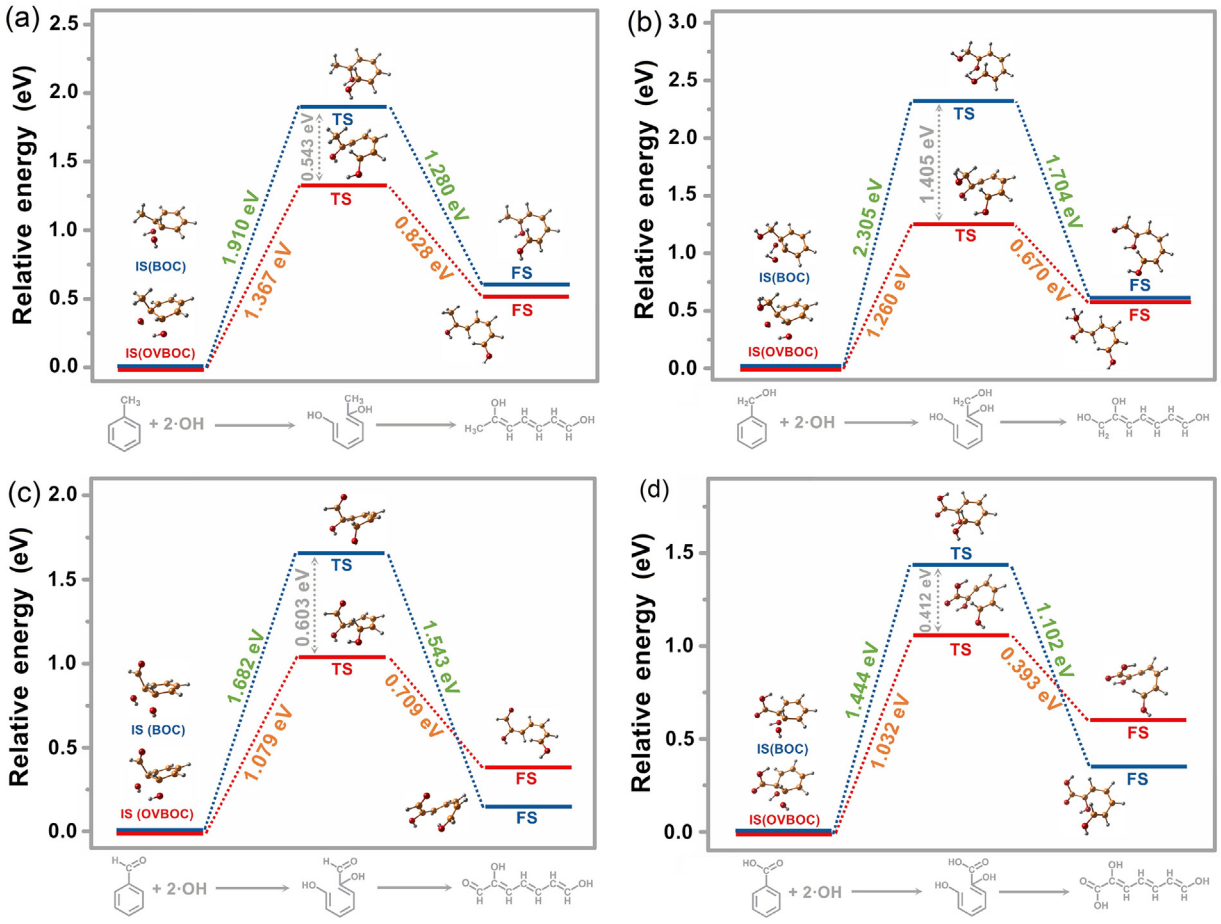

Fig. 5. The calculated NEB reaction pathways for photo-oxidation ring-opening process by ·OH for toluene (a), benzyl alcohol (b), benzaldehyde (c) and benzoic acid (d).

Table 1
Adsorption energies (E_{ads}) of various species on BOC and OVBOC. Negative means heat release for E_{ads}.

Sample	Toluene	Benzyl alcohol	Benzaldehyde	Benzoic acid
BOC	−0.355	−0.424	−0.361	−0.634
OVBOC	−0.671	−0.744	−0.703	−0.968

no significant change appears on benzaldehyde (1,413 and about 1,700 cm^{-1}) and benzoic acid (1,333, 1,382 and 1,501 cm^{-1}) over time, which experimentally identifies that the ring-opening process on OVBOC is mainly started at benzyl alcohol. The ring-opening steps determined by *in situ* DRIFTS well matches with the calculated result. The temporal evolution of normalized absorbance for final mineralized product CO_2 (Fig. 6f) intuitively demonstrates the ring-opening efficiency. The production of CO_2 on OVBOC is more efficient than that on BOC, which further confirms that the toxic intermediates (aromatic oxides and polyhydroxylated compounds) before ring-opening have been greatly suppressed by introducing defects into BOC. The unsaturated long chain enol and alkyne after ring-opening would be quickly degraded into CO_2 and H_2O.

The role of oxygen vacancy in radical production, toluene activation, ring-opening and toxic intermediates control during photocatalytic toluene degradation on defective BiOCl is illustrated in Fig. 7 in detail.

4. Conclusion

In summary, we have proposed and certified that the ring-opening efficiency of toluene photocatalytic degradation can be rationally promoted by oxygen vacancies on the catalyst surface. The combined theoretical calculation and *in situ* DRIFTS results demonstrated that the OVs could enhance the activation of the adsorbed O_2, H_2O and toluene via their localized electrons, offering a new avenue to enhance the thermodynamics toward radicals production and toluene oxidation. The methyl species would be oxidized and tend to open the benzene ring at benzoic acid on BOC while the ring-opening is started at benzyl alcohol on OVBOC. Most importantly, the ring-opening efficiency of photocatalytic toluene degradation can be well boosted because the reaction activation energy of the rate-determining step was significantly reduced by the OVs. Hence, the toxic intermediates (aromatic oxides, epoxides, polyhydroxylated compounds and unsaturated long chain enol) during ring-opening process can be transformed into

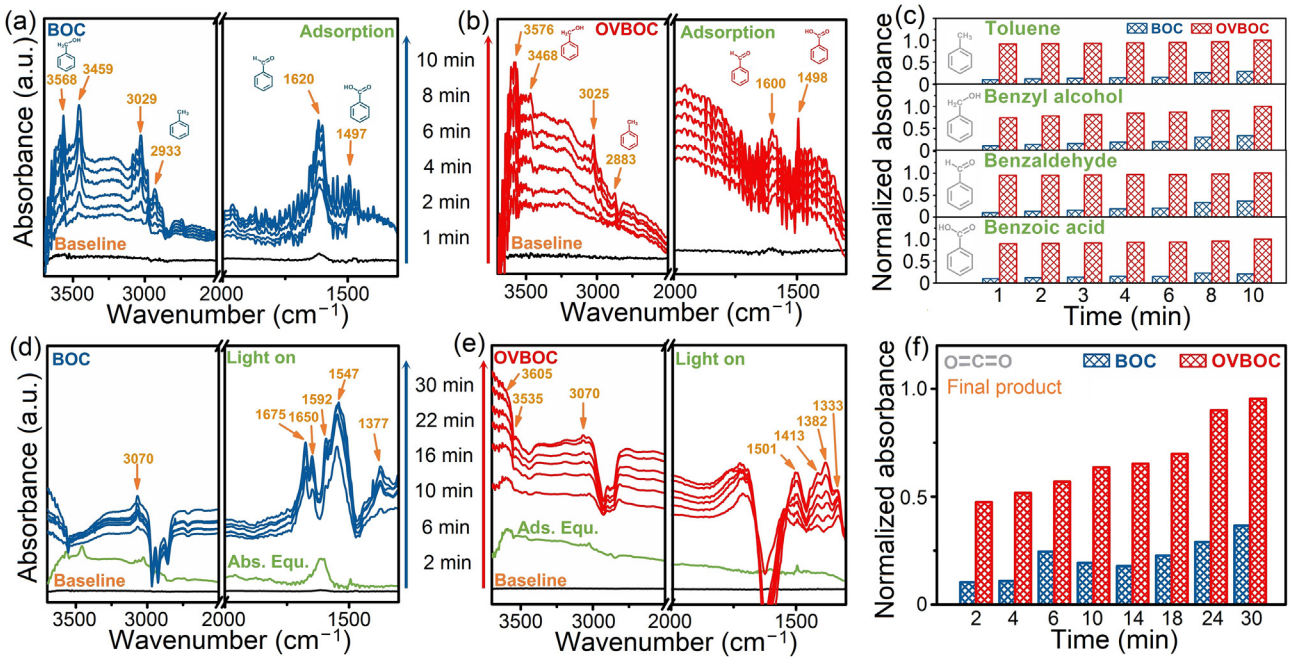

Fig. 6. *In situ* FT-IR spectra of the adsorption process of toluene + O_2 on BOC (a) and OVBOC (b); the photocatalytic degradation of toluene on the surface of BOC (d) and OVBOC (e) under UV light irradiation; species evolution of toluene, benzyl alcohol, benzaldehyde and benzoic acid (c) and CO_2 (f) during the reaction process.

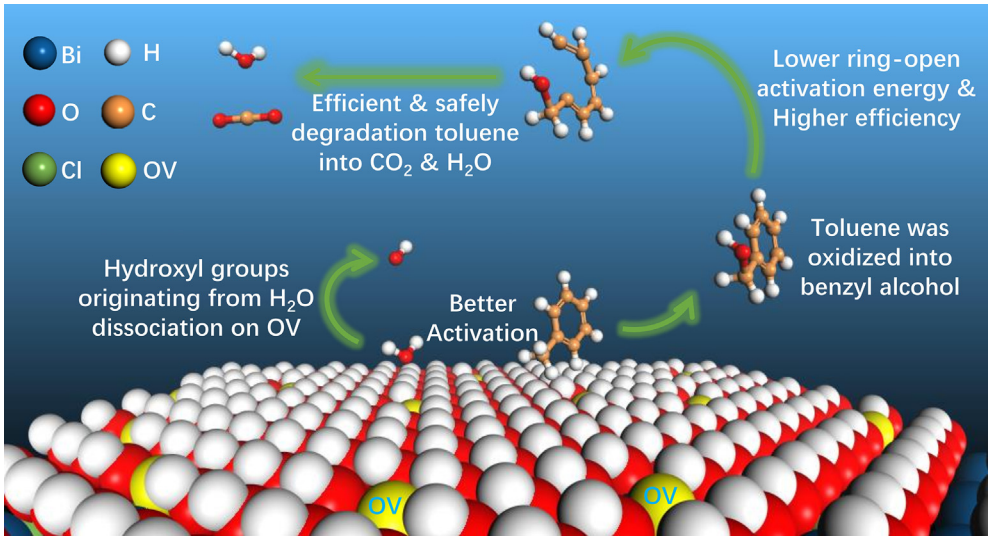

Fig. 7. The illustration of the oxygen vacancy in radicals production, toluene activation, ring-opening and toxic intermediates control during photocatalytic toluene degradation on defective BiOCl.

the final product CO_2 quickly with little toxic products accumulation. These findings highlight the indispensable role of surface defects on toluene degradation and could offer a new strategy for the rational design of new photocatalysts via surface engineering for efficient and safe removal of air pollutants.

Conflict of interest

The authors declare that they have no conflict of interest.

Acknowledgments

This work was supported by the National Key R&D Plan (2016YFC02047), the National Natural Science Foundation of China (21822601, 21777011, and 21501016), the Innovative Research Team of Chongqing (CXTDG201602014), the Key Natural Science Foundation of Chongqing (cstc2017jcyjBX0052), and the Plan for "National Youth Talents" of the Organization Department of the Central Committee. The authors also acknowledge the AM-HPC in Suzhou, China for computational support.

Author contributions

Fan Dong, Hongwei Huang, Yanjuan Sun and Xing'an Dong designed the study. Fan Dong, Haiqiang Wang and Yuxin Zhang provided the support on experimental feasibility. Xing'an Dong, Hong Wang, Wen Cui performed characterization and analysis under the supervision of Fan Dong. Xing'an Dong and Jieyuan Li

performed the VASP calculation. Xing'an Dong wrote the paper. Fan Dong revised the paper. All authors contributed to the interpretation of the results and improvement of the paper.

Appendix A. Supplementary data

Supplementary data to this article can be found online at https://doi.org/10.1016/j.scib.2019.04.020.

References

[1] Streicher HZ, Gabow PA, Moss AH, et al. Syndromes of toluene sniffing in adults. Ann Intern Med 1981;94:758.
[2] Dhada I, Nagar PK, Sharma M. Challenges of TiO_2-based photooxidation of volatile organic compounds: designing, coating, and regenerating catalyst. Ind Eng Chem Res 2015;54:5381–7.
[3] Wang Y, Gu A, Zhang A. Recent development of energy supply and demand in China, and energy sector prospects through 2030. Energ Policy 2011;39:6745–59.
[4] Fujihira M, Satoh Y, Osa T. Heterogeneous photocatalytic oxidation of aromatic compounds on TiO_2. Nature 1981;293:206–8.
[5] Ibusuki T, Takeuchi K. Toluene oxidation on UV-irradiated titanium dioxide with and without O_2, NO_2, or H_2O at ambient temperature. Atmos Environ 1986;20:1711–5.
[6] Obee TN, Brown RT. Photocatalysis for indoor air applications: effects of humidity and trace contaminant levels on the oxidation rates of formaldehyde, toluene, and 1,3-butadiene. Environ Sci Technol 1995;29:1223–31.
[7] Yu KP, Lee GWM. Decomposition of gas-phase toluene by the combination of ozone and photocatalytic oxidation process (TiO_2/UV, TiO_2/UV/O_3, and UV/O_3). Appl Catal B Environ 2007;75:29–38.
[8] Li JY, Dong XA, Zhang G, et al. Probing ring-opening pathways for efficient photocatalytic toluene decomposition. J Mater Chem A 2019;7:3366–74.
[9] Wu ZF, Xiong F, Wang ZM, et al. Thermal-, photo- and electron-induced reactivity of hydrogen species on rutile TiO_2 (110) surface: role of oxygen vacancy. Chin Chem Lett 2018;29:752–6.
[10] Takeuchi M, Hidaka M, Anpo M. Efficient removal of toluene and benzene in gas phase by the TiO_2/Y-Zeolite hybrid photocatalyst. J Hazard Mater 2012;237–238:133–9.
[11] Zhu Y, Wang H, Wang B, et al. Solar thermoelectric field plus photocatalysis for efficient organic synthesis exemplified by toluene to benzoic acid. Appl Catal B Environ 2016;193:151–9.
[12] Zhong L, Brancho JJ, Batterman S, et al. Experimental and modeling study of visible light responsive photocatalytic oxidation (PCO) materials for toluene degradation. Appl Catal B Environ 2017;216:122–32.
[13] Li YH, Sun YJ, Ho WK, et al. Highly enhanced visible-light photocatalytic NO_x purification and conversion pathway on self-structurally modified g-C_3N_4 nanosheets. Sci Bull 2018;63:609–20.
[14] Kong J, Rui Z, Ji HB. Enhanced photocatalytic mineralization of gaseous toluene over $SrTiO_3$ by surface hydroxylation. Ind Eng Chem Res 2016;55:11923–30.
[15] Latriano L, Goldstein BD, Witz G. Formation of muconaldehyde, an open-ring metabolite of benzene, in mouse liver microsomes: an additional pathway for toxic metabolites. Proc Natl Acad Sci USA 1986;83:8356–60.
[16] Burcham PC, Kaminskas LM, Fontaine FR, et al. Aldehyde-sequestering drugs: tools for studying protein damage by lipid peroxidation products. Toxicology 2002;181:229–36.
[17] Dhada I, Nagar PK, Sharma M, et al. Photo-catalytic oxidation technology for VOC control: evaluation and risk characterization of intermediates of benzene degradation adsorbed on catalyst. Eng Sci 2016;33:970–7.
[18] Cao L, Zi G, Suib SL, et al. Photocatalytic oxidation of toluene on nanoscale TiO_2 catalysts: studies of deactivation and regeneration. J Catal 2000;196:253–61.
[19] Wang Q, Liu ZQ, Liu DM, et al. Ultrathin two-dimensional $BiOBr_xI_{1-x}$ solid solution with rich oxygen vacancies for enhanced visible-light-driven photoactivity in environmental remediation. Appl Catal B Environ 2018;236:222–32.
[20] Wang Q, Liu ZQ, Liu DM, et al. Oxygen vacancy-rich ultrathin sulfur-doped bismuth oxybromide nanosheet as a highly efficient visible-light responsive photocatalyst for environmental remediation. Chem Eng J 2019;360:838–47.
[21] Zhao K, Zhang L, Wang J, et al. Surface structure-dependent molecular oxygen activation of BiOCl single-crystalline nanosheets. J Am Chem Soc 2013;135:15750–3.
[22] Chen P, Dong F, Ran MX, et al. Synergistic photo-thermal catalytic NO purification of MnO_x/g-C_3N_4: enhanced performance and reaction mechanism. Chin J Catal 2018;39:619–29.
[23] Sun YJ, Wang H, Xing Q, et al. The pivotal effects of oxygen vacancy on Bi_2MoO_6: promoted visible light photocatalytic activity and reaction mechanism. Chin J Catal 2019;40:647–55.
[24] Wang Y, Chen Z, Han P, et al. Single-atomic cu with multiple oxygen vacancies on ceria for electrocatalytic CO_2 reduction to CH_4. ACS Catal 2018;8:7113–9.
[25] Dvořák F, Szabová L, Johánek V. Bulk hydroxylation and effective water splitting by highly reduced cerium oxide: the role of O vacancy coordination. ACS Catal 2018;8:4354–63.
[26] Dong BB, Liu TF, Li C, et al. Species, engineering and characterizations of defects in TiO_2-based photocatalyst. Chin Chem Lett 2018;29:671–80.
[27] Mao C, Cheng H, Tian H, et al. visible light driven selective oxidation of amines to imines with BiOCl: does oxygen vacancy concentration matter? Appl Catal B Environ 2018;228:87–96.
[28] Schaub R, Wahlström E, Rønnau A, et al. Oxygen-mediated diffusion of oxygen vacancies on the TiO_2 (110) surface. Science 2003;299:377–9.
[29] Setvín M, Aschauer U, Scheiber P, et al. Reaction of O_2 with subsurface oxygen vacancies on TiO_2 anatase (101). Science 2013;341:988–91.
[30] Setvin M, Hulva J, Parkinson GS, et al. Electron transfer between anatase TiO_2 and an O_2 molecule directly observed by atomic force microscopy. Proc Natl Acad Sci USA 2017;114:E2556–62.
[31] Wang B, Wang X, Lu L, et al. Oxygen-vacancy-activated CO_2 splitting over amorphous oxide semiconductor photocatalyst. ACS Catal 2018;8:516–25.
[32] Wang H, He WJ, Dong XA, et al. *In situ* FT-IR investigation on the reaction mechanism of visible light photocatalytic NO oxidation with defective g-C_3N_4. Sci Bull 2018;63:117–25.
[33] Li H, Shi J, Zhao K, et al. Sustainable molecular oxygen activation with oxygen vacancies on the 001 facets of BiOCl nanosheets under solar light. Nanoscale 2014;6:14168–73.
[34] Li H, Shang J, Zhu H, et al. Oxygen vacancy structure associated photocatalytic water oxidation of BiOCl. ACS Catal 2016;6:8276–85.
[35] Li JY, Dong XA, Sun YJ, et al. Tailoring the rate-determining step in photocatalysis via localized excess electrons for efficient and safe air cleaning. Appl Catal B Environ 2018;239:187–95.
[36] Grimme S. Semiempirical GGA-type density functional constructed with a long-range dispersion correction. J Comput Chem 2006;27:1787–99.
[37] Kresse G, Furthm Uuml J. Efficient iterative schemes for Ab initio total-energy calculations using a plane-wave basis set. Phys Rev B Condens Matter 1996;54:11169–86.
[38] Kresse G, Furthmüller J. Efficient iterative schemes for Ab initio total-energy calculations using a plane-wave basis set. Comp Mater Sci 1996;6:15–50.
[39] Perdew JP, Burke K, Ernzerhof M, et al. Generalized gradient approximation made simple. Phys Rev Lett 1996;77:3865–8.
[40] Pe B. Projector augmented-wave method. Phys Rev B: Condens Matter 1994;50:17953–79.
[41] Kresse G, Joubert D. From ultrasoft pseudopotentials to the projector augmented-wave method. Phys Rev B Condens Matter 1999;59:1758–75.
[42] Heyd J. Hybrid functionals based on a screened coulomb potential. J Chem Phys 2003;118:8207–15.
[43] Heyd J. Erratum: "Hybrid functionals based on a screened coulomb potential". J Chem Phys 2006;118:219906.
[44] Henkelman G, Uberuaga BP, Jónsson H. Improved tangent estimate in the nudged elastic band method for finding minimum energy paths and saddle points. J Chem Phys 2000;124:9901–4.
[45] Bader RFW. Atoms in molecules: a quantum theory. Oxford: Oxford University Press; 1994. p. 361–2.
[46] Dong XA, Zhang WD, Sun YJ, et al. Visible-light-induced charge transfer pathway and photocatalysis mechanism on bi semimetal@defective BiOBr hierarchical microspheres. J Catal 2017;357:41–50.
[47] Wang R, Hashimoto K, Fujishima A, et al. Light-induced amphiphilic surfaces. Nature 1997;388:431–2.
[48] Wang R, Hashimoto K, Fujishima A, et al. Photogeneration of highly amphiphilic TiO_2 surfaces. Adv Mater 1998;10:135–8.
[49] Sun R, Nakajima A, Fujishima A. Photoinduced surface wettability conversion of ZnO and TiO_2 thin films. J Phys Chem B 2001;105:1984–90.
[50] Zhou Y, Zhang X, Zhang Q, et al. Role of graphene on the band structure and interfacial interaction of Bi_2WO_6/graphene composites with enhanced photocatalytic oxidation of NO. J Mater Chem A 2014;2:16623–31.
[51] Li JY, Cui W, Sun YJ, et al. Directional electron delivery via a vertical channel between g-C_3N_4 layers promotes photocatalytic efficiency. J Mater Chem A 2017;5:9358–64.
[52] Irokawa Y, Morikawa T, Aoki K, et al. Photodegradation of toluene over $TiO_{2-x}N_x$ under visible light irradiation. Phys Chem Chem Phys 2006;8:1116–21.
[53] Chen LC, Pan GT, Yang TC, et al. *In situ* DRIFT and kinetic studies of photocatalytic degradation on benzene vapor with visiblelight-driven silver vanadates. J Hazard Mater 2010;178:644–51.
[54] Besselmann S, Löffler E, Muhler M. On the role of monomeric vanadyl species in toluene adsorption and oxidation on V_2O_5/TiO_2 catalysts: a Raman and *in situ* DRIFTS study. J Mol Catal A Chem 2000;162:401–11.
[55] Sun S, Ding J, Bao J, et al. Photocatalytic degradation of gaseous toluene on Fe-TiO_2 under visible light irradiation: a study on the structure, activity and deactivation mechanism. Appl Surface Sci 2012;258:5031–7.
[56] He Y, Rui Z, Ji H. *In situ* DRIFTS study on the catalytic oxidation of toluene over V_2O_5/TiO_2 under mild conditions. Catal Commun 2011;14:77–81.
[57] Bartels TT. The sadtler handbook of infrared spectra. Sadtler Res Lab 1978:32.

Xing'an Dong obtained his B.S. degree from Chongqing Technology and Business University (CTBU) in 2019. He is currently a graduate student under the supervision of Prof. Fan Dong at CTBU. His research interests are focused on the design and synthesis of photocatalytic materials for energy and environmental applications.

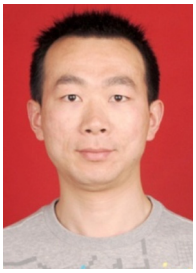

Fan Dong received his Ph.D. degree in 2010 from Zhejiang University. Currently, he is a full professor and director at Institute of Fundamental and Frontier Sciences, University of Electronic Science and Technology of China. His research interests include photocatalysis, environmental and energy catalysis.